ORIGINAL ARTICLE

Journal Section

Intensified reactor for lean methane emissions treatment

Adrian R. Irhamna[1] | **George M. Bollas**[1,*]

[1]Department of Chemical and Biomolecular Engineering, University of Connecticut, Storrs, CT, 06269, USA

Correspondence

George M. Bollas, Department of Chemical and Biomolecular Engineering, University of Connecticut, Storrs, CT, 06269, USA

Email: george.bollas@uconn.edu

The Global Methane Pledge declared at the 2021 United Nations climate change conference (COP26) marked the world's commitment to eradicate methane emissions. Most of these emissions are generated by the oil-gas industry, waste landfills, and agriculture sectors, and are lean in composition. This work explores the use of an intensified reactor that implements the chemical looping principle to handle lean methane emissions. A model-based framework is used to showcase the baseline performance of the proposed reactor in converting methane emissions using nickel-based oxygen carriers. Then, sensitivity analysis of the reactor performance with respect to operating conditions is per-

Abbreviations: CL, chemical-looping; NMVOC, non-methane volatile organic compound; OC, oxygen-carrier; OX, oxidation; RED, reduction.

formed. The reactor is subsequently optimized to minimize the methane emitted, using a dynamic program with safety and operability constraints for the alternating redox process. With the optimal cycle strategy, we demonstrate that near-complete methane conversion can be achieved by the reactor without external heating.

KEYWORDS

Lean methane emissions, reactor design, process intensification, chemical looping, dynamic optimization

1 | INTRODUCTION

An unfortunate common practice in drilling is to reduce the production of greenhouse gas (GHG) emissions by flaring, which burns methane or other unwanted flammable gases that have higher GHG potential than carbon dioxide[1]. In ideal conditions, the performance of a flaring system is excellent and capable of providing over 98 % efficiency[2]. In field operation, however, the performance of a flaring system is often inefficient due to plant disturbances, fuel stream composition variability, and ambient conditions changes[3]. The Environmental Defense Fund (EDF) survey on several flaring sites in the Permian Basin discovered that 11% of flares were unlit and malfunctioning.[4]. Such condition decreases the overall flare efficiency in the Permian Basin to 93%[5], and yields methane emissions at rate of 100 - 200 metric ton/hour[4]. Moreover, the increase in methane emissions is driven by the recent growth of shale gas and biogas production. It is reported that the GHG footprint per Mega Joule of shale gas is about twice that of conventional natural gas, owing to methane emission in the upstream activity of shale gas exploration[6]. A study in the Barnett Shale Region, one of the major shale gas producers in the US, reported that the field released about 544,000 tons of methane a year, which is equal to 46 million tons of CO_2[7]. Scheutz and Fredenslund[8] reported that from

23 biogas plants measurements, a single biogas plant has an overall methane emission rate of 7700 ton CH_4/year, equivalent to CO_2 emission by 1,600 automobiles[9]. Human activities such as livestock production, agriculture, and landfills also contribute emissions of methane, most of which are produced at lean compositions[9]. This methane emissions issue has gained people's awareness lately, and many stakeholders have initiated campaigns on reducing flaring activity for the coming years[10;11]. In the recent 2021 United Nations climate change conference (COP26) in Glasgow, eradicating methane emissions has been declared as a new commitment by the council in the form of the Global Methane Pledge, in which more than 100 countries signed up to reduce methane emissions by at least 30 % by 2030[12].

Chemical-looping (CL) has shown promise in heat generation and reforming applications during the last two decades[13;14;15;16;17;18;19;20;21;22;23;24;25;26]. Due to the separation between air and fuel at the inlet, CL yields downstream gas with high CO_2 concentration such that the stream could be directly guided to CO_2 storage with a less complicated separation unit, and a separate stream of spent air that could be safely released to the atmosphere. The CL process builds upon the ability of an oxygen carrier (OC) to perform redox reactions in separate reactors or reaction stages[16]. Over numerous materials that have been studied as an oxygen carrier, Cu, Mn, Co, Ni, and Fe are the most feasible metals used for the CL process to date[27]. Several terms have been used to classify the CL process based on its particular objective, such as CL combustion[19;28;29;30], CL gasification[31], CL reforming[25;32;33], CL air separation[34;35], or based on how the oxygen is transferred such as chemical looping with oxygen uncoupling (CLOU)[23]. CL has been simulated, modeled, experimented with mainly two different types of reactors, fluidized bed reactors[21;36] and packed (fixed) bed reactors[15;25;36;37]. To date, CL combustion is the most mature and studied CL technology, and stands at the stage of pilot plant operation and demonstration[21;22]. CL has also been diversified for various applications, such as the current effort of employing CL for the production of alternative fuels (hydrogen, syngas, and ammonia[38;25]), chemical products (methanol, ethylene, propylene, formaldehyde, styrene, etc.), or for utilizing biomass material as feed[26]. The exploration of OC materials that have long lifetime, excellent reactivity, and lower cost, is still an area of interest in CL research[27].

This study proposes an intensified process to handle a lean methane emission by adopting the CL principle. A single fixed bed reactor packed with a metal oxygen carrier is designed to perform alternating oxygen carrier redox

reactions with diluted methane from the incoming stream. A fixed bed reactor design is selected due to its simplicity, ability to operate under pressurized conditions and ease in the gas-solid separation. The design of the fixed-bed CL system is based on prior work [17;18;39;40], which was focused on combustion systems for power generation [14;15]. The proposed reactor is described in Figure 1 and uses the exhaust gas from a flare as a case study. In terms of oxygen carrier reactions, there are two main processes occurring in the reactor, the reduction stage of the oxygen carrier and the oxidation stage of the oxygen carrier. Inside the reactor, the diluted methane stream is oxidized into CO_2 and steam via gas-solid reactions with the oxygen carrier during the reduction stage. As air is introduced into the reactor, the process is immediately switched to the oxidation stage, where both the methane and the oxygen carrier are oxidized by the incoming air. Normally, in the traditional CL process, the incoming fuel stream (methane) is separated from the air and only feeds the reduction stage to facilitate the carbon capture technology in the downstream process. In this approach, however, the presence of fuel (methane) stream during the oxidation stage is important to intensify the reactor (providing the heat) and to accommodate the fluctuating and unpredictable flow of the methane released during flaring. Furthermore, the heart of this process lies in the ability of the metal-oxygen carrier to act as a reacting agent, a catalyst, and thermal storage during the overall redox process. Since the overall process is cyclic in a single reactor, the state of the prior stage affects the performance of the following stage. For this reason, management of the heat and cycling of the reactor is essential to achieve autothermal operation.

This work aims to demonstrate a model-based approach to optimally design and control a batch process as an innovative method for treating lean methane emissions. In the beginning, we communicate the model of the CL reactor specifically designed to handle lean methane feed and use the composition of a lean methane emission from flaring as a case study. The reactor is then explored for its baseline performance and characteristics of converting methane to carbon dioxide. A sensitivity analysis of the reactor performance is conducted to study reactor performance as a function of reactor variables and to identify the most significant variables for reactor design. Afterwards, a dynamic optimization problem is formulated to manipulate selected decision variables of the reactor, subject to constraints, and maximize methane conversion. An optimum cycle strategy for the reactor is presented and its performance metrics are compared with the baseline design. We end the study by highlighting key performance benefits, discussing major obstacles, and recommending further improvement options of the proposed reactor design.

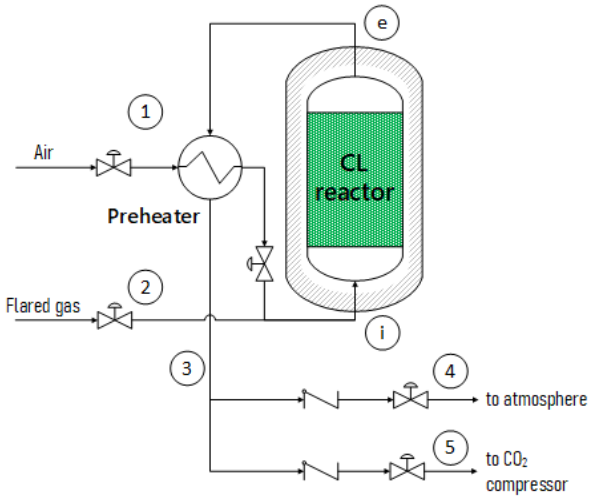

FIGURE 1 Process flow diagram of the conceptual intensified reactor for methane emission treatment.

2 | SYSTEM DESCRIPTION

2.1 | Process Description

The proposed reactor is a fixed bed of a metal oxygen carrier designed to perform reduction and oxidation alternatively. The terms of reduction and oxidation here are based on the redox process experienced by the oxygen carrier in the reactor. The stage of each process is regulated by control valves which govern the incoming air feed as shown in Figure 1. A detailed explanation of the oxygen carrier reduction and oxidation stages is provided in the following paragraphs:

- Reduction stage (Figure 1 index: **2 - i - e - 3 - 5**).

  In this stage, the feed inlet valve (# 2) is open and the air inlet valve (# 1) is closed, allowing the flared gas to flow through the reactor. Inside the reactor, the gas-solid reactions between the flared gas and oxygen carrier reduce the oxygen carrier, yielding an exit gas which mainly consists of CO_2 and steam. Depending on OC, the overall reaction of this stage is usually endothermic. The main heat source is provided by the hot reactor bed which preserves the heat generated during the prior oxidation stage. The exit gas is then used to preheat the incoming

TABLE 1 Emission factors (EF) of flaring emission released in E&P Forum[41;42].

Species	Emission Factor (g/kg of gas flared)
CH_4	35
CO	8.7
CO_2	2610
NO_x	1.5
NMVOC	15
SO_2	0.013

air before it is directed for further processing of steam separation and CO_2 capture. The reduction stage stops when the methane conversion reaches a predetermined lower bound.

- Oxidation stage (Figure 1 index: **1/2 - i - e - 3 - 4**).

In this stage, both inlet valves are open allowing the flared gas and the feed air to flow through the reactor. The presence of air inside the reactor oxidizes the diluted methane in the exhaust stream and regenerates the reduced oxygen carrier. Both of these processes are exothermic, thus the reactor temperature increases during this stage. To accomplish the overall autothermal process, the heat generated during this process is stored in the reactor bed, specifically the metal oxygen carrier, which provides the heat needed for the subsequent reduction stage. Despite their relative insignificance, catalytic gas phase reactions may still occur during this stage. Similar to the reduction stage, before being released to the atmosphere, the exit gas passes through a heat exchanger to preheat the air feed. The product stream from this step, mainly consists of nitrogen and oxygen, and is released into the atmosphere. The oxidation stage stops when there is sufficient heat and oxygen carrier in its oxidized form to satisfy the requirements of the reduction stage.

The flared gas composition used as input to the model is presented in Table 1, and it is taken from a report released by the E&P Forum[41], also cited in[42]. For simplification of the kinetics, the NO_x, SO_2, and Non-methane volatile organic compounds (NMVOC) in the flared gas stream were neglected in this work. The typical flared gas temperature, volumetric flow rate, and flare tip diameter of the flare stack are presented in Table 2.

A fixed bed reactor for this work is developed based on the reactor designed by Han and Bollas in[40] which

TABLE 2 Typical conditions of the flared gas[43].

Flared gas parameter	Value
Flare temperature	650 °C
Flare tip diameter	36 inch
Volumetric flowrate range	40 m^3/s

was later updated in[17] and used for power generation[14;15]. The reactor model was in excellent agreement with literature and in-house experimental data, for a variety of Ni-based OCs, operating conditions and reaction temperatures[39;44;45;46;47;48]. The main difference between the process presented here and prior work is the coexistence of fuel and air in the oxidation stage. This imposes gas-solid reactions, catalytic gas reactions, and methane catalytic combustion to take place during the oxidation stage, and therefore, augments the reactions network. A detailed description of the governing equations and kinetic parameters is provided in Subsections 2.2.1 and 2.2.2, respectively.

2.2 | Reactor Model

2.2.1 | Governing Equations

A heterogeneous dynamic model is used to represent the interactions between gas and the solid particles in the CL reactor. The reactor is modeled as adiabatic and one-dimensional; thus, radial temperature and concentration gradients are neglected. The dynamic mass and energy balances for the fluid phase are shown in the Eqs. (1) and (2), respectively:

$$\epsilon_b \frac{\partial C_i}{\partial t} + \frac{\partial F_i}{\partial V} = \epsilon_b \frac{\partial}{\partial z}\left(D_{\mathrm{ax},i} \frac{\partial C_i}{\partial z}\right) + k_{c,i} a_v \left(C_{c,i}\big|_{r=r_c} - C_i\right), \tag{1}$$

$$(\epsilon_b C_{p,f} C_T + (1-\epsilon_b)\rho_c C_{p,c})\frac{\partial T}{\partial t} + C_{p,f} F_T \frac{\partial T}{\partial V} = \epsilon_b \frac{\partial}{\partial z}\left(\lambda_{\text{ax}} \frac{\partial T}{\partial z}\right) + h_f a_v \left(T_c\big|_{r=r_c} - T\right), \tag{2}$$

where t is the process time, z is the axial dimension of the reactor, ϵ_b is the bed porosity, C_i is the concentration of gas species i in the fluid phase, C_T is the total concentration of the bulk fluid, F_i is the molar flow rate of gas species i, V is the volume of the observed fluid, D_{ax} is the axial dispersion coefficient of species i, $k_{c,i}$ is the mass transfer coefficient between the bulk fluid and that on the surface of oxygen carrier particles, a_v is the external particle surface area per unit volume, $C_{c,i}$ is the concentration of gas species i in the solid phase, $C_{p,f}$ is the heat capacity of the bulk gas mixture, T is the bulk fluid temperature, F_T is the total molar gas flow, λ_{ax} is the axial heat dispersion coefficient, h_f is the heat transfer coefficient between the bulk fluid and oxygen carrier particles, T_c is the solid phase temperature, and r_c is the radius of the solid particle. The mass and energy balance of the fluid phase apply Danckwertz boundary conditions as shown in the Eqs. (3) - (5),

$$\epsilon_b D_{\text{ax},i} \frac{\partial C_i}{\partial z}\bigg|_{z=0} = [u(C_i - C_{i,\text{in}})]\big|_{z=0}, \tag{3}$$

$$\epsilon_b \lambda_{\text{ax}} \frac{\partial T}{\partial z}\bigg|_{z=0} = [u C_T C_{p,f}(T - T_{\text{in}})]\big|_{z=0}, \tag{4}$$

$$\frac{\partial C_i}{\partial z}\bigg|_{z=L} = \frac{\partial T}{\partial z}\bigg|_{z=L} = 0, \tag{5}$$

where u is the velocity of the bulk fluid, $C_{i,\text{in}}$ is the inlet concentration of gas species i, and T_{in} is the inlet temperature of the bulk fluid.

Given the low CH_4 concentration and relatively low temperature, the reactor inlet during oxidation is modelled

as an unreacted mixture of fuel (flared gas) and the added air. The inlet temperature of the mixture of inlet flared gas and air is calculated by Eq. (6).

$$T_{m,0} = \frac{F_{\text{flare}} C_{p,\text{flare}} T_{\text{flare}} + F_{\text{air}} C_{p,\text{air}} T_{\text{air}}}{F_{\text{flare}} C_{p,\text{flare}} + F_{\text{air}} C_{p,\text{air}}}, \tag{6}$$

where $T_{m,0}$ is the mixture inlet temperature, F_{flare}, the molar flowrate, $C_{p,\text{flare}}$, the heat capacity, and T_{flare}, are the temperature of the inlet flared gas, respectively, and F_{air}, the molar flowrate, $C_{p,\text{air}}$, the heat capacity, and T_{air}, are the temperature of the inlet air, respectively.

For the solid phase in the reactor, the dusty-gas model describes the mass transfer of the concentrated gas-solid flow within the OC particle. Assuming OC particles of spherical shape, the dynamic mass balance of the gas phase inside a particle is:

$$\epsilon_c \frac{\partial C_{c,i}}{\partial t} + \frac{1}{r^2} \frac{\partial}{\partial r} (r^2 J_i) = \rho_{c,s} \sum R_i, \tag{7}$$

where r is the radial element of the particle, $C_{c,i}$ is the concentration of gas species i inside the particle, J_i is the flux of gas species i, R_i is the intrinsic rates of reactions species i involved in the reactor, $\rho_{c,s}$ is the density of solid part of oxygen carrier. The flux of gas species, J_i, through a solid particle is:

$$-\frac{\partial C_{c,i}}{\partial r} = \sum_{i=1, j \neq i}^{N} \frac{1}{D_{ij}^e} (y_j J_i - y_i J_j) + \frac{J_i}{D_{iK}^e}, \tag{8}$$

where D^e_{ij} is the effective binary molecular diffusivity of gas species i in the gas species j, D^e_{iK} is the effective Knudsen diffusivity, y_i is mole fraction of the species i, and N is the total number of gas species in the particle. Both the effective binary molecular and the Knudsen diffusivity coefficients are functions of the void space in the particle, ϵ_c, and the tortuosity, τ, as shown in the Eqs. (9) and (10):

$$D^e_{ij} = \frac{\epsilon_c}{\tau} D_{ij}, \tag{9}$$

$$D^e_{iK} = \frac{\epsilon_c}{\tau} D_{iK}. \tag{10}$$

The small pores in the particle lead to an assumption of negligible convective forces and pressure gradients inside the particle [17]. The boundary conditions for the dusty gas and particle model are:

$$J_i\big|_{r=0} = 0, \tag{11}$$

$$J_i\big|_{r=r_c} = k_{c,i}\left(C_{c,i}\big|_{r=r_c} - C_i\right). \tag{12}$$

Temperature gradients inside a particle are due to conductive heat and the heat generation or consumption due to reactions. The energy balance of the particle is expressed by Fourier's law:

$$\begin{aligned}((1-\epsilon_c)\rho_c C_{p,c} + \epsilon_c C_{p,fc} C_{T,c})\frac{\partial T_c}{\partial t} = \\ \frac{1}{r^2}\frac{\partial}{\partial r}\left(r^2 \lambda_c \frac{\partial T_c}{\partial r}\right) + \rho_{c,s}\sum_{n=1}^{N_n}(-\Delta H_n)(R_n),\end{aligned} \tag{13}$$

where $C_{p,c}$ is the heat capacity of the solid, $C_{p,fc}$ is the heat capacity of the bulk gas mixture in the particle, $C_{T,c}$ is the total concentration of bulk gas mixture in the particle, λ_c is the thermal conductivity of solid phase, and ΔH_n is the heat of reaction n. The energy balance of the particle is constrained by the following boundary conditions:

$$\left.\frac{\partial T_c}{\partial r}\right|_{r=0} = 0, \tag{14}$$

$$-\lambda_s \left.\frac{\partial T_c}{\partial r}\right|_{r=r_c} = h_f\left(T_c\big|_{r=r_c} - T\right). \tag{15}$$

The momentum balance in the reactor is assumed as pseudo-steady state and dominated by friction forces. Pressure drop across the reactor is calculated using the Ergun equation:

$$\frac{dP}{dz} = -\left(\frac{1-\epsilon_b}{\epsilon_b^3}\right)\left(\frac{\rho u_0^2}{d_c}\right)\left(\frac{150}{Re_c} + 1.75\right), \tag{16}$$

where P is the total pressure in the bed, u_0 is the superficial gas velocity at the inlet, d_c is the diameter of the oxygen carrier particle, and Re_c is the particle Reynolds number:

$$Re_c = \frac{\rho u_0 d_c}{(1-\epsilon_b)\,\mu}, \tag{17}$$

where μ is the dynamic viscosity of the bulk gas. The boundary conditions for the momentum balance are:

$$P\big|_{z=0} = P_0, \tag{18}$$

$$P\big|_{z=L} = P_{\text{out}}. \tag{19}$$

More details on the model including the correlations for process parameters (i.e., heat capacities, diffusion coefficients, solid properties) can be found in Han et al.[40;49].

2.2.2 | Kinetic Model

The model adopts the kinetic model of nickel-based oxygen carrier that has been extensively studied and validated in[39;44;45;46;47;48]. The kinetic model was initially studied by Zhou et al.[44;39], who recommended a set of gas-solid reaction kinetics for Cu and Ni oxygen carriers. Han et al.[40;49] then investigated the interparticle and intraparticle diffusion effects of oxygen carriers of variable size. Structural identifiability analysis and optimal experimental design derived the minimal, most information-rich kinetic model in[47;48]. The kinetic model[48] was extended for high pressure processes[50], up to 10 atm[46]. The reactions and kinetic rates for Ni oxygen carrier reduction are provided in Tables 3 and 4, respectively. These gas-solid and catalytic reactions between the feed and the Ni oxygen carrier (Reactions 1 - 9 in the Table 3 and 4) are retained in the oxidation stage to facilitate the presence of the flared gas. In addition, the reaction and rate of methane combustion from[51] are introduced in the oxidation stage to account for the overall combustion reaction of methane with air. The complete list of kinetic rates for the oxidation stage are presented in the Tables 3 and 4, respectively. The pre-exponential factor, activation energy, equilibrium constants, and adsorption coefficients are provided in Tables 5 and 6.

TABLE 3 List of reactions feasible in the reduction and oxidation stages of the chemical-looping system

Index	Reactions		
(R1)	$H_2 + NiO$	$\longrightarrow$	$Ni + H_2O$
(R2)	$CO + NiO$	$\longrightarrow$	$Ni + CO_2$
(R3)	$CH_4 + NiO$	$\longrightarrow$	$Ni + 2\,H_2 + CO$
(R4)	$CH_4 + H_2O$	$\rightleftharpoons$	$3\,H_2 + CO$
(R5)	$CO + H_2O$	$\rightleftharpoons$	$H_2 + CO_2$
(R6)	$CH_4 + CO_2$	$\rightleftharpoons$	$2\,CO + 2\,H_2$
(R7)	CH_4	$\rightleftharpoons$	$2\,H_2 + C$
(R8)	$C + H_2O$	$\rightleftharpoons$	$CO + H_2$
(R9)	$C + CO_2$	$\rightleftharpoons$	$2\,CO$
(R10)	$O_2 + 2\,Ni$	$\longrightarrow$	$2\,NiO$
(R11)	$O_2 + C$	$\longrightarrow$	CO_2
(R12)	$O_2 + 2\,C$	$\longrightarrow$	$2\,CO$
(R13)	$O_2 + 2\,CO$	$\longrightarrow$	$2\,CO_2$
(R14)	$CH_4 + 2\,O_2$	$\longrightarrow$	$CO_2 + H_2O$

TABLE 4 Kinetic parameters for reaction in Table 3

Index	Rate of reaction expression
(R1)	$R_1 = a_0 k_1 / P^{1.39} n (1 - X_{NiO})(-\ln(1 - X_{NiO}))^{1-1/n} C_{H_2} C'_{NiO}$
(R2)	$R_2 = a_0 k_2 / P^{1.21} n X (1 - X_{NiO})(-\ln(1 - X_{NiO}))^{1-1/n} C_{CO} C'_{NiO}$
(R3)	$R_3 = a_0 k_5 / P^{1.01} n (1 - X_{NiO})(-\ln(1 - X_{NiO}))^{1-1/n} C_{CH_4} C'_{NiO}$
(R4)	$R_4 = \frac{a_0}{P} \frac{k_4}{P_{H_2}^{2.5}} \left(P_{CH_4} P_{H_2O} - \frac{P_{H_2}^3 P_{CO}}{K_4} \right) C'_{Ni} \Big/ \left(1 + K_{CO,4} P_{CO} + K_{H_2,4} P_{H_2} + K_{CH_4,4} P_{CH_4} + \frac{K_{H_2O,4} P_{H_2O}}{P_{H_2}} \right)^2$
(R5)	$R_5 = \frac{a_0}{P} \frac{k_5}{P_{H_2}} \left(P_{CO} P_{H_2O} - \frac{P_{H_2} P_{CO_2}}{K_5} \right) C'_{Ni} \Big/ \left(1 + K_{CO,5} P_{CO} + K_{H_2,5} P_{H_2} + K_{CH_4,5} P_{CH_4} + \frac{K_{H_2O,5} P_{H_2O}}{P_{H_2}} \right)^2$
(R6)	$R_6 = \frac{a_0}{P} k_6 K_{CH_4,6} \left(P_{CH_4} P_{CO_2} - \frac{P_{CO}^2 P_{H_2}^2}{K_6} \right) C'_{Ni} \Big/ \left(1 + K_{CH_4,6} P_{CH_4} \right)$
(R7)	$R_7 = a_0 k_7 K_{CH_4,7} \left(P_{CH_4} - \frac{P_{H_2}^2}{K_7} \right) C'_{Ni} \Big/ \left(1 + \frac{P_{H_2}^{3/2}}{K_{H_2,7}} + K_{CH_4,7} P_{CH_4} \right)$
(R8)	$R_8 = a_0 \frac{k_8}{K_{H_2O,8}} \left(P_{H_2O} P_{H_2} - \frac{P_{CO} P_{H_2}^2}{K_8} \right) C_C C'_{Ni} \Big/ \left(P_{H_2} + K_{CH_4,8} P_{CH_4} P_{H_2} + \frac{P_{H_2O}}{K_{H_2O,8}} + \frac{P_{H_2}^{2.5}}{K_{H_2,8}} \right)^2$
(R9)	$R_9 = a_0 \frac{k_9}{K_{CO,9} K_{CO_2,9}} \left(P_{CO_2} P_{CO} - \frac{P_{CO}^3}{K_9} \right) C_C C'_{Ni} \Big/ \left(P_{CO} + K_{CO,9} P_{CO}^2 + \frac{P_{CO_2}}{K_{CO,9} K_{CO_2,9}} \right)^2$
(R10)	$R_{10} = a_0 k_{10} / P^{1.02} (1 - X_{Ni})^{2/3} (1 - X_{Ni}) C_{O_2} C'_{Ni}$
(R11)	$R_{11} = a_0 k_{11} / P (1 - X_C) P_{O_2} C'_C$
(R12)	$R_{12} = a_0 k_{12} / P (1 - X_C) P_{O_2} C'_C$
(R13)	$R_{13} = a_0 k_{13} C_{O_2} C_{CO} C'_{Ni} \Big/ (1 + K_{CO,13} C_{CO})^2$
(R14)	$R_{14} = k_{14} P_{CH_4} P_{O_2}^{0.5} \Big/ \left(1 + K_{CH_4,14} P_{CH_4} + K_{O_2,14} P_{O_2}^{0.5} \right)^2$

TABLE 5 Pre-exponential factor (A) and activation energy (Ea) of the kinetic rate constant for reaction n

Index	A_n	Ea_n [kJ/mol]	Index	A_n	Ea_n [kJ/mol]
(R1)	7.70E-02 [$\frac{bar^{1.16}m}{s}$]	27	(R8)	7.10E-01 [$\frac{mol}{m^2 s}$]	132
(R2)	4.22E-04 [$\frac{bar^{0.81}m}{s}$]	37	(R9)	1.47E+13 [$\frac{mol}{m^2 s}$]	365
(R3)	2.32E-04 [$\frac{bar^{1.01}m}{s}$]	39	(R10)	1.38E-03 [$\frac{bar^{1.2}m}{s}$]	22
(R4)	1.01E+05 [$\frac{mol \cdot bar^{1.5}}{m^2 s}$]	168	(R11)	2.06E+02 [$\frac{m}{s}$]	99
(R5)	7.25E+01 [$\frac{mol}{m^2 s}$]	102	(R12)	4.88E+03 [$\frac{m}{s}$]	127
(R6)	9.21E-01 [$\frac{mol}{m^2 s}$]	124	(R13)	5.80E+09 [$\frac{bar \cdot m^6}{mol \cdot kg \cdot s}$]	120
(R7)	7.00E-01 [$\frac{mol}{m^2 s}$]	59	(R14)	3.287E+02 [$\frac{mol}{kg \cdot s \cdot bar^{1.5}}$]	30.8

Kinetic rate constant expression of reaction n

For (R1) to (R3): $k_n = A_n \exp(\frac{Ea_n}{R}\left(\frac{1}{T_c} - \frac{1}{T_{ref}}\right))$, and for (R4) to (R14): $k_n = A_n \exp(\frac{Ea_n}{RT_c})$, where T_c is the temperature of the bed in [K] and T_{ref} = 973K

TABLE 6 Reaction equilibrium constants and adsorption coefficients for the reactions with NiO oxygen carrier

Kinetic variables	(R4)	(R5)	(R6)	(R7)	(R8)	(R9)	(R13)	(R14)
$K_{n,0}$	1.2E+13 [bar^2]	1.77E-02	6.78E+14 [bar^2]	2.98E+05 [bar]	4.02E+07 [bar]	2.28E+09 [bar]	–	–
$\Delta H_{n,0}$ [kJ/mol]	268	-36.6	260	84.4	139	175	–	–
$K_{CH_4,n,0}$	6.65E-04 [bar^{-1}]	6.65E-04 [bar^{-1}]	4.04E-04 [bar^{-1}]	2.1E-01 [bar^{-1}]	3.49 [bar^{-1}]	–	–	2.02E-3 [bar^{-1}]
$\Delta H_{CH_4,n,0}$ [kJ/mol]	-38.3	-38.3	-74.6	0.567	–	–	–	36.3
$K_{H_2,q,0}$	6.12E-09 [bar^{-1}]	6.12E-09 [bar^{-1}]	–	5.18E+07 [bar$^{3/2}$]	1.83E+13 [bar$^{2.5}$]	–	–	–
$\Delta H_{H_2,n,0}$ [kJ/mol]	-82.9	-82.9	–	133	216	–	–	–
$K_{CO,n,0}$	8.23E-05 [bar^{-1}]	8.23E-5 [bar^{-1}]	–	–	4.73E-06	7.34E-06 [bar^{-1}]	5.22 [m^3/mol]	–
$\Delta H_{CO,n,0}$ [kJ/mol]	-70.6	-70.6	–	–	-97.8	-100.4	8.37	–
$K_{H_2O,n,0}$	1.77E+05	1.77E+05	–	–	– [bar]	–	–	–
$\Delta H_{H_2O,n,0}$ [kJ/mol]	88.7	88.7	–	–	–	–	–	–
$K_{CO_2,n,0}$	–	–	–	–	–	8.17E+07 [bar]	–	7.45E-05 [bar$^{-0.5}$]
$\Delta H_{CO_2,n,0}$ [kJ/mol]	–	–	–	–	–	104	–	57.9

Equilibrium constant, $K_n = K_{n,0} \exp\left(-\frac{\Delta H_{n,0}}{RT}\right)$, and **Adsorption coefficient**, $K_{i,n} = K_{i,n,0} \exp\left(-\frac{\Delta H_{i,n,0}}{RT}\right)$

3 | DYNAMIC SIMULATION OF THE BASELINE DESIGN

In this section, we study the performance of the reactor with a baseline design. The baseline reactor is designed for the flare composition and flow rate presented in the Tables 1 and 2. In the baseline design, the diameter and the length of the reactor were selected by considering the volumetric flow rate of the flared gas, to yield sufficient residence time for the reactions, and the pressure drop inside the reactor. Ambient air is selected as the feed added during the oxidation stage. It is assumed that the Ni-based oxygen carrier is initially in its oxide form (NiO). The summary of the baseline design parameters is shown in Table 7. With this baseline design, the reactor performance is evaluated at two different conditions: (1) when it acts as a simple reducer (without the oxidation stage), and (2) when it performs repeated alternative redox cycles until cyclic steady-state. The dynamic simulation of the baseline design is started from the reduction stage. The dynamic simulation results of the baseline design acting as a simple reducer and that of 24 minutes of the redox cyclic steady state (which includes two redox cycles) are presented in Figures 2 and 3, respectively.

Figure 2(a) shows the methane conversion inside the reactor after 6.7 hours. The total methane conversion in the reducer is near 100 %, which is confirmed in Figure 2(b). Despite the reactor being able to convert about 97 % of methane, it is interesting to note that H_2 and CO are detected at the reactor exit, which indicates the dominance of catalytic reactions. The catalytic reactions in the reactor are caused by the Ni saturation in the bed (Figure 2(d)) owing to extensive reduction of the OC. In Figure 2(c), it is observed that the temperature of the reactor bed drops from 650 °C at the inlet to 600 °C at the outlet due to the endothermic nature of the reduction and reforming. Ni saturation and temperature drop in this reducer showcase the significance of the oxidation stage in the proposed reactor to regenerate the oxygen carrier and to provide the heat for the overall process.

Figure 3(a) shows that at cyclic steady-state, methane is completely converted during the oxidation stage, while about 93 % of methane is converted at the reduction stage. This is emphasized by Figure 3(b) as no methane is detected at the reactor exit during the oxidation stage. The higher methane conversion in the oxidation stage was due to the rapid combustion reaction between methane and oxygen and that between methane and the oxidized OC. Syngas (H_2 and CO) was undetected at the exit implying that there was always sufficient oxygen in the reactor for

TABLE 7 Reactor configuration and operating condition of the baseline design

Reactor parameters	Value
Reactor Diameter (m)	10
Length-to-Diameter Ratio, L/D	0.25
Volumetric flowrate of flared gas (m^3/s)	40
Temperature of flared gas (°C)	650
Flared gas composition (% mole)	
CH_4	1.2
H_2O	65.6
CO	0.2
CO_2	32.7
Air-to-Flared gas ratio	0.6
Temperature of air ($°C$)	25
Air composition (% mole)	80 N_2; 20 O_2
OC percentage (%)	5
Reduction; Oxidation time (s)	375 ; 225
Time Horizon (h)	3.3

their oxidation. This is confirmed by the excess oxygen leaving the reactor (Figure 3(b)) and the domination of NiO in the reactor bed (Figure 3(d)). The exit gas temperature was around 750 °C, higher than that in the reducer reactor (Figure 2(c)) and was relatively constant despite the alternate switching of redox processes. This was due to the heat front that is generated during the oxidation stage being pushed to the end of the reactor and distributed evenly in the bed (Figure 3(c)).

4 | SENSITIVITY ANALYSIS

Before optimizing the reactor design, we performed sensitivity analysis to identify variables of significance to the reactor performance. For this sensitivity analysis, 4 reactor performance metrics were evaluated: methane conversion, bed temperature, bed NiO conversion, and the ratio of CO_2 production-to-CH_4 feed. These performance metrics

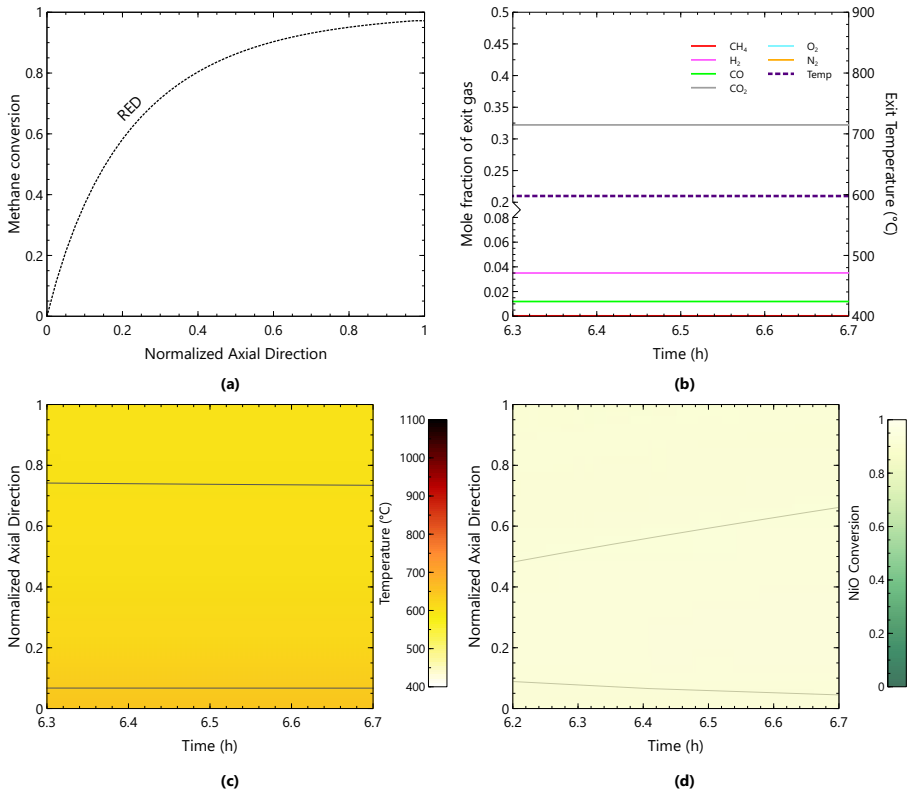

FIGURE 2 Reactor performance of the baseline design (Table 7) as a reducer: (a) methane conversion inside the reactor at the end of 6.7 hours; (b) species mole fraction and temperature at the reactor exit - H_2O and CO_2 plot are not visible in this plot due to their large quantity at the exit stream; (c) temperature contour plot of the reactor bed; and (d) NiO conversion contour plot of the reactor bed - conversion of 0 refers to NiO and conversion of 1 refers to Ni.

were evaluated with respect to 5 independent variables of the reactor: NiO loading, Reactor Length, Feed Air Temperature, Ratio of Air-to-Flared Gas, and Ratio of Oxidation-to-Reduction Step Time. For each sensitivity analysis, an independent variable is varied while keeping other variables at the baseline design values (Table 7). The results of the sensitivity analysis are presented in Figure 4 for the methane conversion, Figure 5 for the bed temperature, Figure 6 for NiO conversion, and Figure 7 for the ratio of CO_2 production-to-CH_4 feed.

Figure 4 shows that methane conversion is more sensitive to the NiO loading and reactor length than the other three variables. Figure 4(a) shows that methane conversion is proportional to the amount of NiO inside the bed, as NiO and Ni promote gas-solid and catalytic reactions. The reactor length has similar effect on methane conversion, as

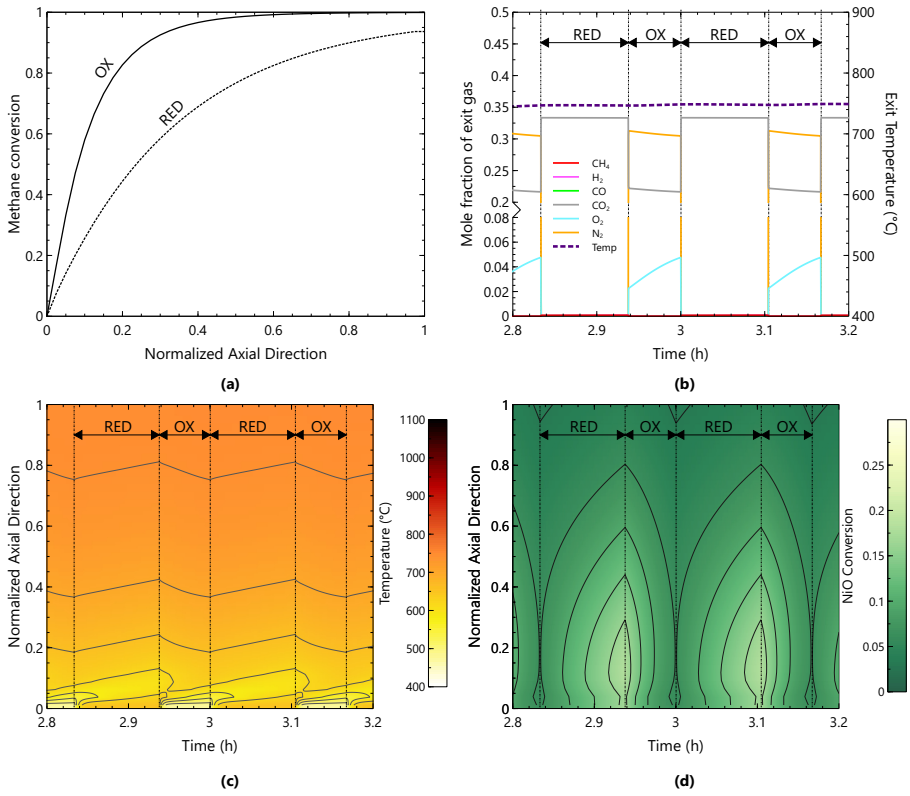

FIGURE 3 Reactor performance of the baseline design (Table 7) at the cyclic steady state condition: (a) methane conversion inside the reactor at the end of reduction and oxidation stage; (b) species mole fraction and temperature at the reactor exit - N_2, H_2O, and CO_2 are not visible in this plot due to their large quantity at the exit stream; (c) temperature contour plot of the reactor bed; and (d) NiO conversion contour plot of the reactor bed - conversion of 0 refers to NiO and conversion of 1 refers to Ni.

it practically increases the amount of NiO and Ni available in the reactor and the residence time of the stream. Figure 4(c) shows that methane conversion is relatively insensitive towards the change of the feed air temperature. Generally, high-temperature feed air increases the overall bed temperature which enhances the rate of the gas-solid and catalytic reactions. The ratio of air-to-flared gas (AFR) and the ratio of the oxidation-to-reduction period (α), shown in Figures 4(d) and 4(e), respectively, represent the intensity and the duration of the oxidation stage. Both figures indicate that methane conversion decreases as more ambient air is injected into the reactor. Excessive ambient air and extensive oxidation stages cool down the reactor, Figure 5(d), which eventually lowers methane conversion. On the other hand, with less air injected into the reactor or a swift oxidation stage, less heat is generated in the reactor which is insufficient

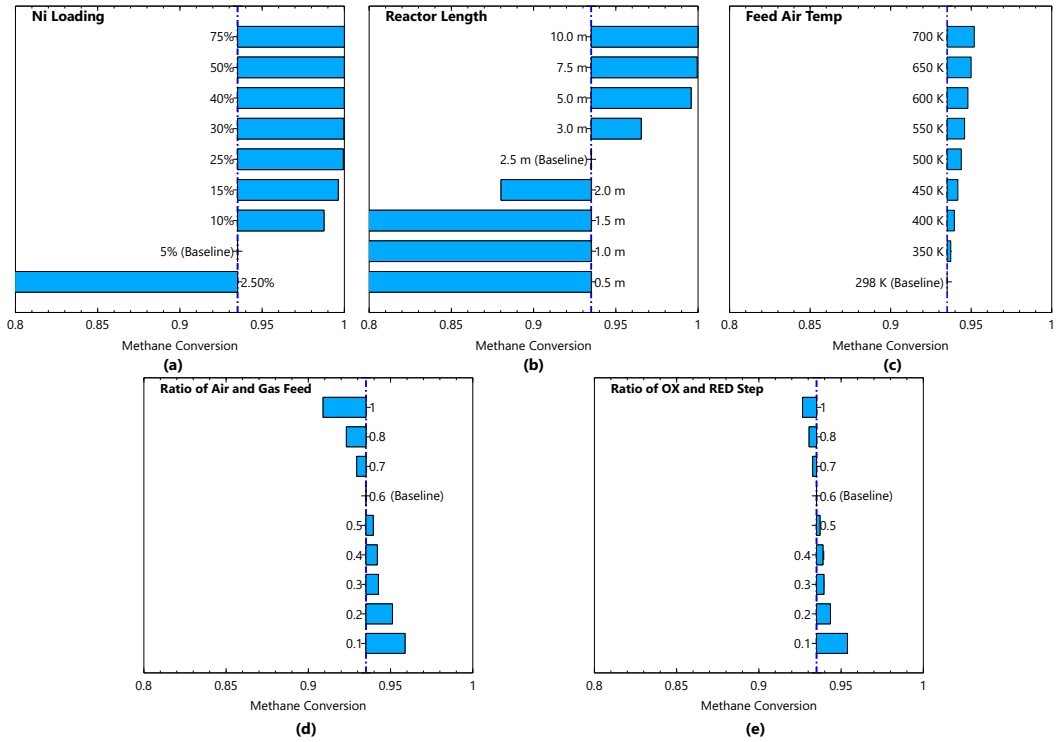

FIGURE 4 Sensitivity analysis of methane conversion with respect to (a) Ni loading; (b) reactor length; (c) feed air temperature; (d) ratio of air to flared gas (AFR); (e) ratio of oxidation to reduction stage (α)

to maintain the bed at its reactive temperature. Figures 4(d) and 4(e), however, show that more methane is converted at the lower AFR and α. Ni catalytic reactions dominate during the reduction stage, as there was limited oxygen available to regenerate the oxygen carrier. Thus, the reactor operates, as the reducer of Figure 2, releasing H_2 and CO.

Figure 5 shows that all of the selected independent variables have significant effect on the mean bed temperature of the reactor. In Figure 5(a), the mean bed temperature of the reactor resembles the trends of methane conversion, as NiO enhances the oxidation reactions that generate more heat. As for the reactor length, shown in Figure 5(b), the highest mean bed temperature is achieved at around 2.5 - 3.0 m, close to the baseline design. Longer reactors do not heat up, while shorter reactors accomplish limited oxidation reactions. In Figure 5(c), we can see that the mean bed temperature is strongly associated with the feed air temperature, as prescribed by the overall reactor energy balance. Figures 5(d) and 5(e) demonstrate that the effects of feed air and the oxidation stage duration on the mean

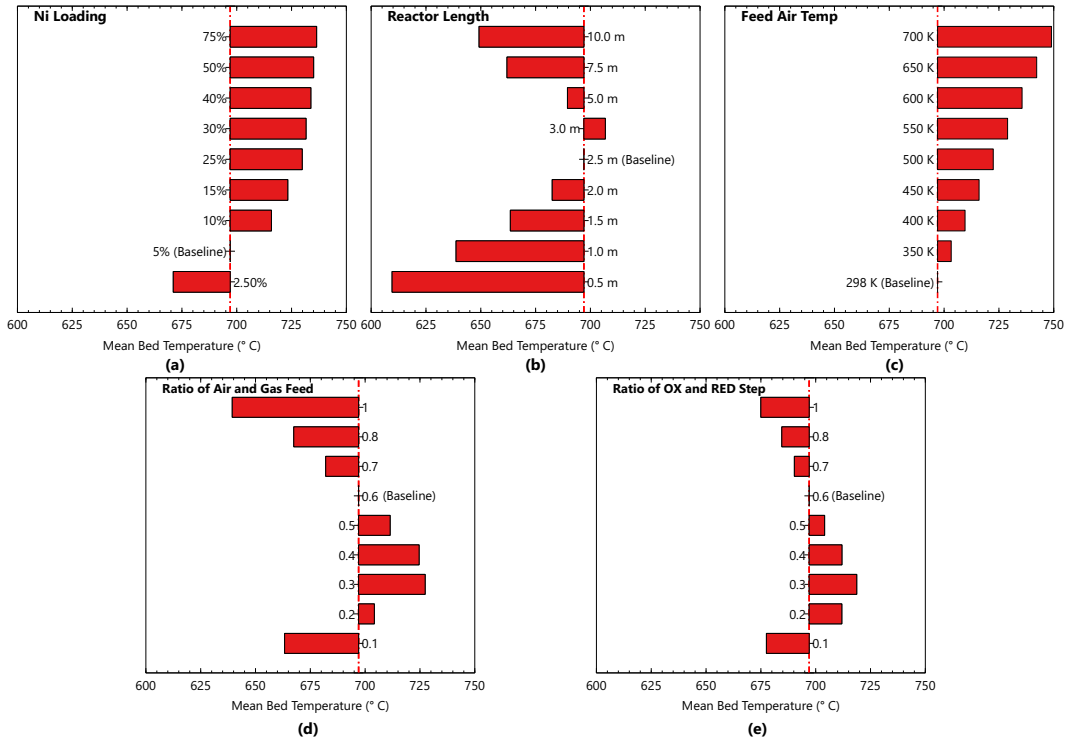

FIGURE 5 Sensitivity analysis of mean bed temperature with respect to (a) Ni loading; (b) reactor length; (c) feed air temperature; (d) ratio of air to flared gas (AFR); (e) ratio of oxidation to reduction stage (α)

bed temperature are substantial and show an optimal value within 0.2 - 0.4 range of these two variables. As discussed in the previous paragraph, both feed air and oxidation period are critical to maintaining the reactor temperature during the redox process. Less feed air or short oxidation times generate less heat during the oxidation stage, which lowers the mean bed temperature. On the other hand, excess of air fed or extended oxidation times cool down the reactor.

Figure 6 shows that the mean bed NiO conversion is impacted by all independent variables, except for the feed air temperature. In Figures 6(a) and (b), the effect of NiO loading and reactor length are inversely proportional to the overall NiO conversion, as expected. Figure 6(c) shows that the overall NiO conversion is insensitive to the overall the feed air temperature. The higher mean bed temperature due to higher feed air temperature (Figure 5(c)) only increases the reaction front in the reactor but still results in the same overall NiO conversion. Figure S2 in Supplementary Information confirms that with higher feed air temperature, higher NiO conversion occurs near the reactor entrance while lower NiO conversion occurs at the middle and exit of the reactor, which results in a relatively similar overall

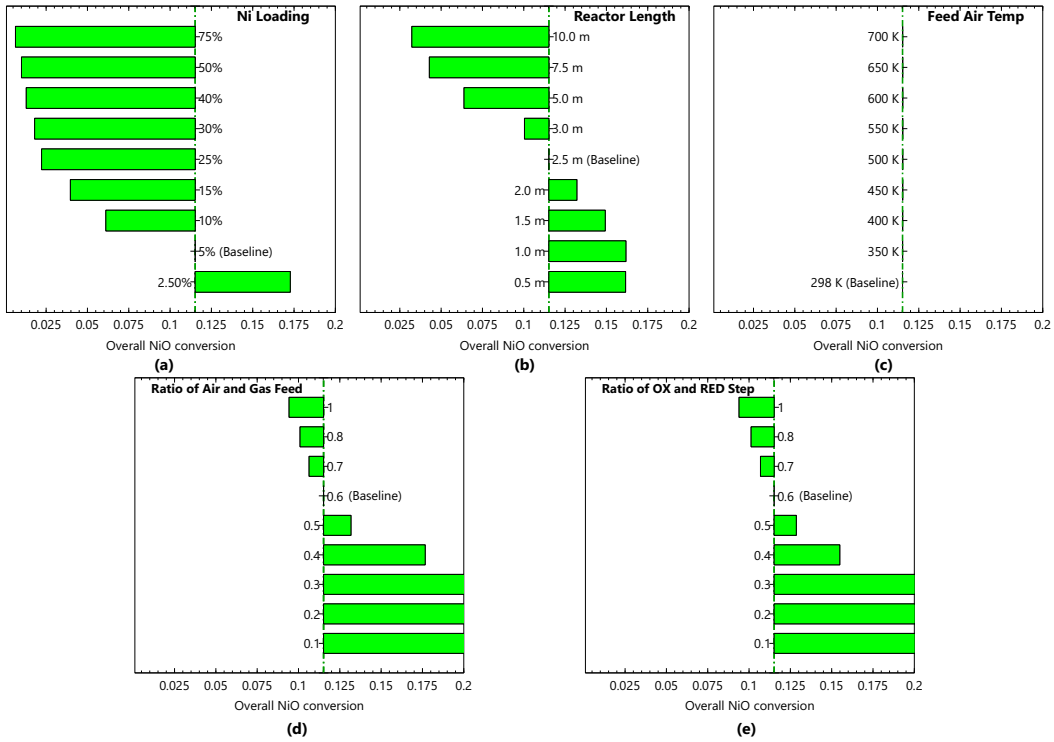

FIGURE 6 Sensitivity analysis of NiO conversion with respect to (a) Ni loading; (b) reactor length; (c) feed air temperature; (d) ratio of air to flared gas (AFR); (e) ratio of oxidation to reduction stage (α)

NiO conversion to that with lower feed air temperature. In Figures 6(d) and 6(e), the overall NiO conversion is shown to be inversely proportional to the feed air and oxidation period. As mentioned in the sensitivity analysis of methane conversion (Figures 4(d) and (e)), less feed air or swift oxidation stage result in more Ni in the reactor bed (increased NiO conversion), while more feed air or prolonged oxidation stage result in more NiO in the bed (lower NiO conversion).

Figure 7 shows the sensitivity analysis of methane converted to CO_2. Figure 7(a)-(c) shows the same pattern as Figure 4(a)-(c), demonstrating that methane was converted to CO_2 at most scenarios studied. As discussed previously, more oxygen carrier and higher bed temperature enhance the conversion of methane to CO_2. Figure 7(d) shows a different pattern than Figure 4(d) at the lower AFR. At this condition, the reactor bed is saturated with Ni and catalytic reactions become dominant cracking methane to syngas, suppressing the production of CO_2. Figure 7(e) also shows a different pattern than Figure 4(e) at the longer oxidation stage. As the oxidation period is extended, more carbon from the incoming methane stream is oxidized to higher CO_2 yield at the exit.

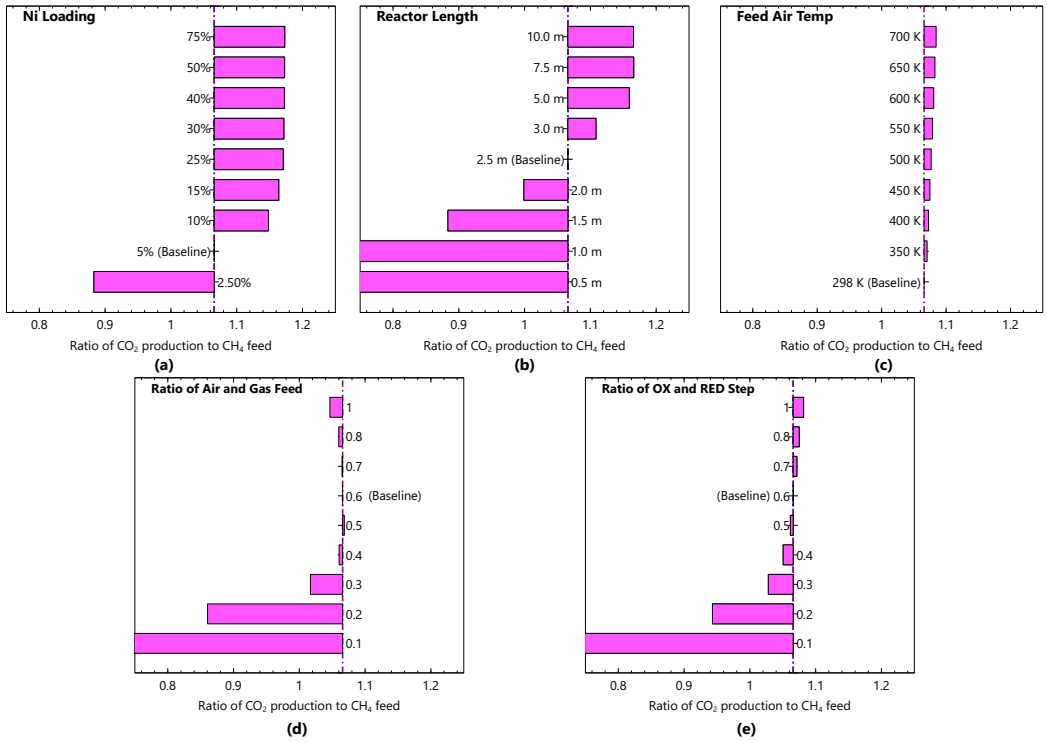

FIGURE 7 Sensitivity analysis of ratio of CO_2 production to the CH_4 input with respect to (a) Ni loading; (b) reactor length; (c) feed air temperature; (d) ratio of air to flared gas (AFR); (e) ratio of oxidation to reduction stage (α)

In summary, the variables chosen for the sensitivity analysis influence the reactor performance metrics differently. NiO loading and reactor length have relatively similar patterns for all reactor performance metrics as both represent the density of oxygen carrier in the bed. The presence of oxygen carrier proportionally affects all of the reactor performance metrics. Higher feed air temperature improves almost all reactor performance metrics, except for the oxygen carrier conversion. Both the AFR and oxidation period show non-monotonic effects on reactor performance metrics, and must be tuned. For these reasons, we select 4 independent variables: NiO loading; Feed Air Temperature; Ratio of Feed Air-to-Flared Gas; Ratio of Oxidation-to-Reduction Step, as the design variables for reactor optimization.

5 | OPTIMIZATION

5.1 | Optimization Formulation

For reactor design optimization, other than the design variables discussed in the sensitivity analysis, we added the reduction time interval as a design variable since it controls the extent of methane conversion and the balance between reduction, reforming, and carbon formation reactions[17;18]. The summary of the design variables used for reactor optimization are presented in Table 8.

TABLE 8 Design variables of the proposed reactor for the optimization problem

Design variables	Notations
Air-to-flared gas ratio	AFR
Feed air temperature	T_{air}
Reduction time interval	δ_{RED}
Ratio of oxidation-to-reduction interval	α
Metal oxide content in oxygen carrier	ω

Since the feed air is only available during the oxidation stage, we defined piecewise constant functions, $\mathbf{u}$, for AFR and T_{air} in the optimization formulation as follows:

$$\mathbf{u} = [AFR, T_{\text{air}}]. \tag{20}$$

As for the other design variables, the reduction interval, δ_{RED}, and the oxidation interval, represented by α, are considered as control variables, while the metal oxide content in oxygen carrier, ω, is a time-invariant design variable. The set of control and design variables are summarized in the design vector, ϕ, shown in Eq. (21):

$$\phi = [\mathbf{u}, \delta_{\text{RED}}, \alpha, \omega] \in \mathbf{\Phi}. \tag{21}$$

During optimization, the design vector, ϕ, is manipulated to maximize the objective function. The objective function for this study is the time-integral of the ratio of the exit molar flow rate of CO_2 over methane feed flowrate, γ, as shown in Eq. (22):

$$\gamma = \int_{t_0}^{t_f} \frac{F_{\text{out,CO}_2}}{F_{\text{in,CH}_4}} dt. \tag{22}$$

The optimization is constrained by other reasonable performance metrics. First, the reactor should be able to convert at least 98 % of the methane to comply with the EPA recommendation [52]. Also, the mean temperature of the reactor bed is expected to be above 700 °C to ensure the reactivity of the oxygen carrier [53]. However, the maximum temperature at any point in the reactor has to be below 1100 °C to avoid sintering of the oxygen carrier [53]. The feed air temperature is constrained between 100 °C and 427 °C to ensure feasibility of preheating the air. Lastly, the ratio between pressure drop and inlet pressure must be below 15% to avoid additional compressing [43]. The complete formulation of the discussed optimization problem is shown in Eq. (23):

$$
\begin{aligned}
&\max_{\phi \in \mathbf{\Phi}} \gamma \\
&\text{subject to:} \\
&\mathbf{f}(\dot{\mathbf{x}}(t), \mathbf{x}(t), \mathbf{u}(t), \theta, t) = 0, \\
&\mathbf{f}_0(\dot{\mathbf{x}}(t_0), \mathbf{x}(t_0), \mathbf{u}(t_0), \theta, t_0) = 0, \\
&T(t_i, z) - 1100^{\circ}\mathrm{C} \leq 0, \quad \forall\, t \in [t_0, t_f], \\
&700^{\circ}\mathrm{C} - \frac{1}{L} \cdot \int_{z=0}^{z=L} T(t_i, z)\, dz \leq 0, \quad \forall\, t \in [t_0, t_f], \\
&100^{\circ}\mathrm{C} - T_{\mathrm{air}} \leq 0, \\
&T_{\mathrm{air}} - 427^{\circ}\mathrm{C} \leq 0, \\
&\Delta P(t)/P(t, z=0) - 15\% \leq 0, \quad \forall\, t \in [t_0, t_f], \\
&\mathbf{x}^{\min} \leq \mathbf{x}(t) \leq \mathbf{x}^{\max}, \\
&\mathbf{u}^{\min} \leq \mathbf{u} \leq \mathbf{u}^{\max}, \\
&\delta_{\mathrm{RED}}^{\min} \leq \delta_{\mathrm{RED}} \leq \delta_{\mathrm{RED}}^{\max}, \\
&\alpha^{\min} \leq \alpha \leq \alpha^{\max}, \\
&\omega^{\min} \leq \omega \leq \omega^{\max}.
\end{aligned}
\tag{23}
$$

In Eq. (23), **f** is the set of differential-algebraic equations (DAEs) representing the reactor model discussed in the Subsection 2.2; **x** is the vector of state variables (*i.e.*, mass, temperature, and pressure); and θ is the system parameters, including kinetic constants, describing the reactivity of oxygen carrier. The mathematical model was developed and solved in the commercial software gPROMS[54]. The set of DAEs was solved with the non-linear solver DASOLV[55]. The non-linear optimization was solved with control vector parameterization with single shooting (CVP_SS algorithm). With control vector parameterization, the control variables were discretized as piecewise constant over a specified

time interval, while with the single shooting approach, the control variables are fixed during the entire time horizon in each iteration.

5.2 | Optimization Result

The optimization problem stated in Eq. (23) was solved and yielded the result presented in Table 9. In the optimal conditions, the oxygen carrier loading and feed air temperature are higher than the baseline design as both are proportional to the methane conversion to CO_2 as discussed in the sensitivity analysis. Meanwhile, the value of reduction time, AFR, and α, were tuned to maximize methane conversion to CO_2. The reactor performance at cyclic steady state with the optimal operating conditions is presented in Figure 8.

TABLE 9 Optimized design varibles of the reactor solved from Eq. (23)

Decision variables	Optimized Value	Lower bound	Upper bound
Air-to-flared gas ratio, AFR	**0.9746**	0.4	1
Temperature of feed air, T_{air} (°C)	**426.85**	100	426.85
Reduction time, δ_{RED} (s)	**322.331**	200	1000
Ratio of Oxidation-to-Reduction time, α	**0.5544**	0.4	1
NiO loading, ω (%)	**17.674**	10	40

Figure 8(a) shows that near-complete methane conversion ($>$ 99%) is achieved during both reduction and oxidation. More than 95 % of methane is converted at the first half of the reactor, faster than that of the baseline design, Figure 3(a). Near-complete methane conversion is confirmed in Figure 8(b), as no methane is detected at the reactor exit either during reduction or oxidation. Methane conversion to CO_2 is also verified as syngas is not detected at the reactor exit. This high methane conversion is mainly due to the higher NiO loading in the reactor which increase the extent of CO_2 producing reactions. Furthermore, the higher NiO concentration in the bed promote the oxidation reactions which generate more heat and increase the overall bed temperature. Figure 8(c) shows that the bed has a uniform temperature close to 780 °C from 30 % of reactor length to the reactor exit, higher than that of the baseline design, Figure 3(c). The main temperature gradient occurs at the first 30 % of reactor length, where the main reaction front takes place. Figure 8(d) shows that only a small fraction of NiO is converted to Ni during reduction. However,

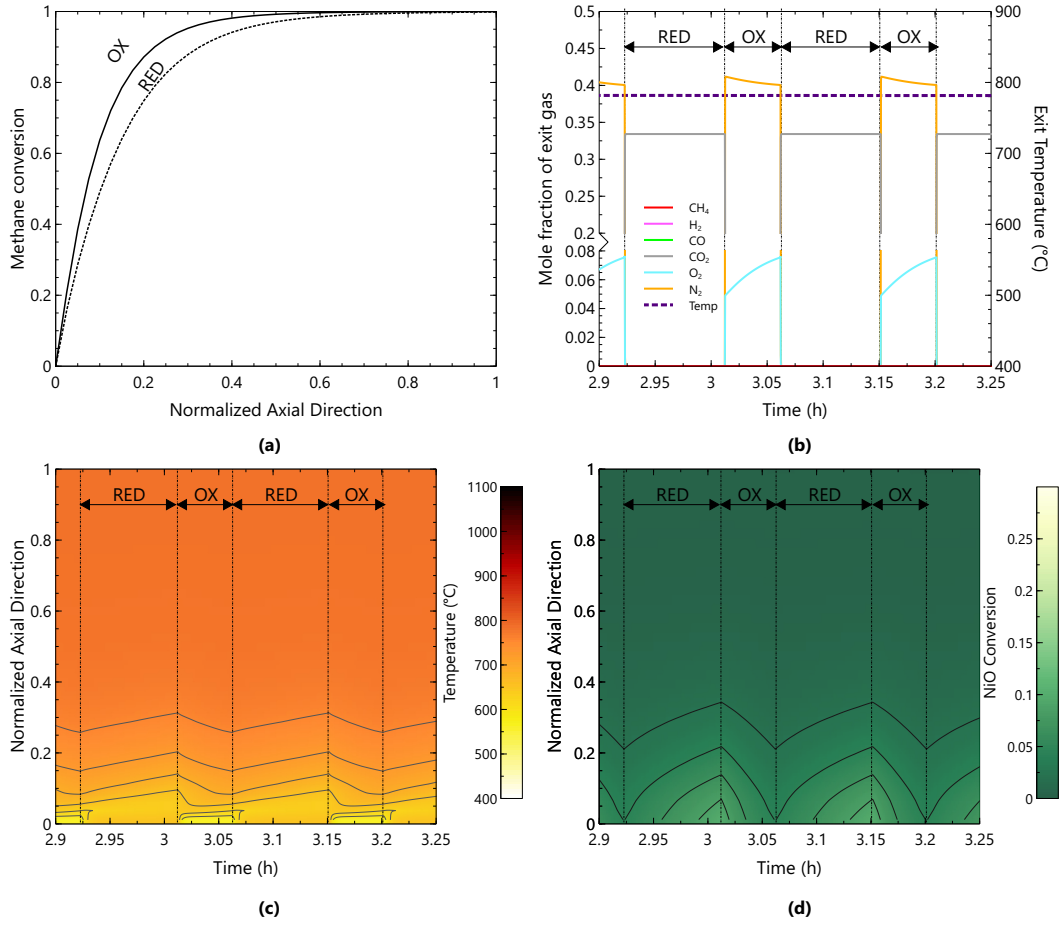

FIGURE 8 Reactor performance of optimized optimal reactor design and control (Table 9) at cyclic steady state: (a) methane conversion inside the reactor at the last cycle of the process; (b) the species mole fraction and temperature at the reactor exit. N_2, H_2O, and CO_2 are invisible in this plot due to their large fraction at the exit stream; (c) temperature contour plot of the reactor bed; and (d) NiO conversion contour of reactor bed - conversion of 0 refers to NiO and conversion of 1 refers to Ni.

the coupling of the exothermic Ni oxidation reactions with those of reduction, help preserve the methane oxidation reactions to CO_2, which were infeasible without the redox cycling of the OC. The bed serves as a heat sink, where reactions that are exothermic increase the temperature sufficiently for the near-complete conversion of methane.

6 | CONCLUSIONS

In this study, we explored the use of an intensified reactor based on the chemical-looping concept to convert lean methane emissions to carbon dioxide. The performance of a baseline design showed that the reactor requires an alternating redox process to intensify the reactor and to manage the heat and reaction front. A sensitivity analysis of the reactor concluded that the oxygen carrier loading, the feed air temperature, air-to-flared gas ratio, and the intervals of reduction and oxidation stages are crucial factors for the control of the reactor performance. These factors were used as design and control variables to solve a dynamic optimization problem that maximizes lean methane conversion to carbon dioxide. At the optimal design, complete methane conversion to CO_2 was achieved by the reactor at cyclic steady state. With an optimal heat management and cycling strategy, the reactor could maintain heat and reaction fronts that are self-sustained and alternate for the complete conversion of methane. The main reaction occurs at the first one-third of the reactor creating a dynamic cycling between reduction-oxidation states of the OC. The challenge of this design is the requirement of a wide reactor diameter to provide sufficient residence time for the feed gas, which might not always be feasible. This issue can be addressed by utilizing several identical reactors with smaller diameter in parallel.

Notations

Greek letters

α	ratio of the oxidation-to-reduction interval
$\mathbf{\Phi}$	design space
ϕ	design vector
θ	vector of system parameters
δ_{RED}	reduction time interval [s]
ϵ_b	bed porosity
ϵ_c	particle porosity
γ	ratio of time-integral of the exit molar flow rate of CO_2 to time-integral of methane feed
λ_{ax}	axial heat dispersion coefficient [$W/(mK)$]
λ_c	thermal conductivity of solid phase [$W/(mK)$]
μ	dynamic viscocity of the gas mixture [Ns/m^2]
ω	metal oxide content in oxygen carrier
ρ	density of the gas mixture [kg/m^3]
ρ_c	density of the oxygen carrier [kg/m^3]
$\rho_{c,s}$	density of the solid part of oxygen carrier, $\rho_{c,s} = \rho_c/(1-\epsilon_c)$, [$kg/m^3$]
τ	particle tortuosity

General symbols

ΔH_n	heat of reaction n [J/mol]
ΔP	pressure drop between outlet and inlet of the reactor [bar]
$\mathbf{f}$	set of differential algebraic equations
$\mathbf{u}$	piecewise constant function used in optimization
$\mathbf{u}$	vector of time-varying control variable
$\mathbf{x}$	vector of state variables: mass, temperature, and pressure

361 a_0 initial specific surface area of the oxygen carrier [m^2/kgOC]

362 A_n pre-exponential factor of reaction n

363 a_v external particle surface area per unit volume [m^{-1}]

364 AFR air-to-flared gas ratio

365 C'_{NiO} initial concentration of NiO per oxygen carrier weight [kgNiO/kg OC]

366 C_i concentration of gas species i in fluid phase [mol/m^3]

367 C_T total gas concentration in fluid phase [mol/m^3]

368 C_{NiO} NiO concentration per oxygen carrier weight [kgNiO/kg OC]

369 C_{Ni} Ni concentration per oxygen carrier weight [kgNiO/kg OC]

370 $C_{c,i}$ concentration of gas species i in the solid phase [mol/m^3]

371 $C_{i,in}$ inlet concentration of the gas species i [mol/m^3]

372 $C_{p,air}$ heat capacity of the inlet air [J/(mol K)]

373 $C_{p,flare}$ heat capacity of the inlet flared gas [J/(mol K)]

374 $C_{p,c}$ heat capacity of the solid [J/(mol K)]

375 $C_{p,fc}$ heat capacity of the gas mixture in the solid phase [J/(mol K)]

376 $C_{p,f}$ heat capacity of the gas mixture in the fluid phase [J/(mol K)]

377 $C_{p,i}$ heat capacity of the gas species i [J/(molK)]

378 $C_{T,c}$ total gas concentration in solid phase [mol/m^3]

379 D diameter of reactor [m]

380 d_c diameter of the oxygen carrier particle [m]

381 $D_{ax,i}$ axial dispersion coefficient of species i [m^2/s]

382 D^e_{ij} effective binary molecular diffusivity of gas species i in the gas species j [cm^2/s]

383 D^e_{iK} effective Knudsen diffusifity of species i [m^2/s]

384 Ea_n energy activation of reaction n

385 F_i molar flow rate of the species i [mol/s]

386 F_T total molar gas flow [mol/s]

387 F_{air} molar flowrate of the inlet air [mol/s]

388 F_{flare} molar flow rate of the inlet flared gas [mol/s]

389 $F_{in,i}$ Inlet molar flowrate of species i [mol/s]

390 $F_{out,i}$ Exit molar flowrate of species i [mol/s]

391 h_f heat transfer coefficient between bulk fluid and oxygen carrier particles [$W/(m^2K)$]

392 i, j gas phase species (CH_4, H_2, H_2O, CO, CO_2, Ar, N_2, O_2)

393 J_i flux of gas species i [$mol/(m^2s)$]

394 K_n equilibrium constant for reaction n

395 k_n rate constant of reaction n

396 $k_{c,i}$ mass transfer coefficient between the bulk fluid and oxygen carrier particles [m/s]

397 $K_{i,n}$ adsorption coefficient of gas species i for reaction n

398 L length of the reactor [m]

399 N total gas species existed in the particle

400 n chemical reactions

401 P total pressure [bar]

402 P_i partial pressure of species i [bar]

403 Q_0 inlet volumetric flowrate into the reactor[m^3/s]

404 r radial element of the particle

405 r_c radius of the solid particle [m]

406 R_i rate of production or consumption of species i [$mol/(m^3s)$]

407 R_n rate of reaction n [$mol/(m^3s)$]

408 Re_c Reynolds number of the particle

409 T bulk fluid temperature [K]

410 t time [s], [h]

411 T_c temperature of the solid phase [K]

412 T_0 inlet temperature of the bulk fluid [K]

413 T_{air} temperature of the inlet air [K]

414 T_{flare} temperature of the inlet flared gas [K]

415 T_{in} inlet temperature of the bulk fluid [K]

416 T_{ref} reference temperature for kinetic rate constant expression [K]

417 $T_{m,0}$ mixture temperature between inlet flared gas and air [K]

418 u velocity of the bulk fluid [m/s]

419 u_0 superficial velocity at the inlet [m/s]

420 V volumetric element

421 V_R volume of the reactor [m^3]

422 X conversion of oxygen carrier from NiO to Ni

423 X_{CH_4} methane conversion

424 X_{NiO} conversion of oxygen carrier from Ni to NiO

425 y_i mole fraction of gas species i

426 z axial element of the reactor

427 References

428 1. Ohio EPA: Division of Air Pollution Control . Understanding the Basics of Gas Flaring. Tech. Rep. November, Ohio Envi-
429 ronmental Protection Agency; Columbus, OH: 2014. https://epa.ohio.gov/. Accessed August 1, 2022.

430 2. Caulton DR, Shepson PB, Cambaliza MO, McCabe D, Baum E, Stirm BH. Methane destruction efficiency of natural
431 gas flares associated with shale formation wells. *Environmental Science and Technology* 2014; 48(16): 9548–9554. doi:
432 10.1021/es500511w

433 3. Strosher M. Investigations of flare gas emissions in Alberta. tech. rep., Environmental Technologies Alberta Research
434 Council; Calgary,Alberta: 1996.

435 4. Permian Methane Analysis Project. tech. rep., Environmental Defense Fund; Austin, TX: .
436 https://data.permianmap.org/pages/flaring. Accessed November 18 2021.

437 5. Gaffney Cline . Tackling Flaring : Learnings from Leading Permian Operators. tech. rep., Environmental Defense Fund; New

York, NY: 2020. https://business.edf.org/insights/tackling-flaring-learnings-from-leading-permian-operators/. Accessed August 1 2022.

6. Howarth R. Methane emissions and climatic warming risk from hydraulic fracturing and shale gas development: implications for policy. *Energy and Emission Control Technologies* 2015: 45. doi: 10.2147/eect.s61539

7. Yacovitch TI, Herndon SC, Pétron G, et al. Mobile Laboratory Observations of Methane Emissions in the Barnett Shale Region. *Environmental Science and Technology* 2015; 49(13): 7889–7895. doi: 10.1021/es506352j

8. Scheutz C, Fredenslund AM. Total methane emission rates and losses from 23 biogas plants. *Waste Management* 2019; 97: 38–46. doi: 10.1016/j.wasman.2019.07.029

9. EPA . Greenhouse Gas Emissions from a Typical Passenger Vehicle. online; 2018. https://www.epa.gov/greenvehicles/greenhouse-gas-emissions-typical-passenger-vehicle. Accessed August 1 2022.

10. IEA . Flaring Emissions. online; 2021. https://www.iea.org/reports/flaring-emissions. Accessed November 5 2022.

11. World Bank . Zero Routine Flaring by 2030. online; 2022. https://www.worldbank.org/en/programs/zero-routine-flaring-by-2030. Accessed November 7 2021.

12. COP26: EU helps deliver outcome to keep the Paris Agreement targets alive. Tech. Rep. November, European Comission; Glasgow: 2021. https://ec.europa.eu/commission/presscorner/detail/en /ip_21_6021. Accessed March 15 2022.

13. Adanez J, Abad A, Garcia-Labiano F, Gayan P, De Diego LF. Progress in chemical-looping combustion and reforming technologies. *Progress in Energy and Combustion Science* 2012; 38(2): 215–282. doi: 10.1016/j.pecs.2011.09.001

14. Chen C, Bollas GM. Optimal design of combined cycle power plants with fixed-bed chemical-looping combustion reactors. *AIChE Journal* 2019; 65(7). doi: 10.1002/aic.16516

15. Chen C, Bollas GM. Design and Scheduling of Semibatch Chemical-Looping Reactors. *Industrial and Engineering Chemistry Research* 2020; 59(15): 6994–7006. doi: 10.1021/acs.iecr.9b05693

16. Fan LS, Li F. Chemical looping technology and its fossil energy conversion applications. *Industrial and Engineering Chemistry Research* 2010; 49(21): 10200–10211. doi: 10.1021/ie1005542

17. Han L, Bollas GM. Chemical-looping combustion in a reverse-flow fixed bed reactor. *Energy* 2016; 102: 669–681. doi: 10.1016/j.energy.2016.02.057

18. Han L, Bollas GM. Dynamic optimization of fixed bed chemical-looping combustion processes. *Energy* 2016; 112: 1107–1119. doi: 10.1016/j.energy.2016.07.031

19. Jin H, Ishida M. Reactivity study on a novel hydrogen fueled chemical-looping combustion. *International Journal of Non-Linear Mechanics* 2001; 36(8): 889–894.

20. Li F, Fan LS. Clean coal conversion processes - Progress and challenges. *Energy and Environmental Science* 2008; 1(2): 248–267. doi: 10.1039/b809218b

21. Lyngfelt A, Brink A, Langørgen Ø, Mattisson T, Rydén M, Linderholm C. $11,000$h of chemical-looping combustion operation — Where are we and where do we want to go?. *International Journal of Greenhouse Gas Control* 2019; 88(May): 38–56. doi: 10.1016/j.ijggc.2019.05.023

22. Lyngfelt A. Chemical Looping Combustion: Status and Development Challenges. *Energy and Fuels* 2020; 34(8): 9077–9093. doi: 10.1021/acs.energyfuels.0c01454

23. Mattisson T, Lyngfelt A, Leion H. Chemical-looping with oxygen uncoupling for combustion of solid fuels. *International Journal of Greenhouse Gas Control* 2009; 3(1): 11–19. doi: 10.1016/j.ijggc.2008.06.002

24. Moghtaderi B. Review of the recent chemical looping process developments for novel energy and fuel applications. *Energy and Fuels* 2012; 26(1): 15–40. doi: 10.1021/ef201303d

25. Spallina V, Marinello B, Gallucci F, Romano MC, Van Sint Annaland M. Chemical looping reforming in packed-bed reactors: Modelling, experimental validation and large-scale reactor design. *Fuel Processing Technology* 2017; 156: 156–170. doi: 10.1016/j.fuproc.2016.10.014

26. Zhu X, Imtiaz Q, Donat F, Müller CR, Li F. Chemical looping beyond combustion-a perspective. *Energy and Environmental Science* 2020; 13(3): 772–804. doi: 10.1039/c9ee03793d

27. Qasim M, Ayoub M, Ghazali NA, Aqsha A, Ameen M. Recent Advances and Development of Various Oxygen Carriers for the Chemical Looping Combustion Process: A Review. *Industrial and Engineering Chemistry Research* 2021; 60(24): 8621–8641. doi: 10.1021/acs.iecr.1c01111

28. Ishida M, Zheng D, Akehata T. Evaluation of a chemical-looping-combustion power-generation system by graphic exergy analysis. *Energy* 1987; 12(2): 147–154. doi: 10.1016/0360-5442(87)90119-8

29. Ishida M, Jin H. A new advanced power-generation system using chemical-looping combustion. *Energy* 1994; 19(4): 415–422. doi: 10.1016/0360-5442(94)90120-1

30. Ishida M, Jin H. A novel chemical-looping combustor without NOx formation. *Industrial and Engineering Chemistry Research* 1996; 35(7): 2469–2472. doi: 10.1021/ie950680s

31. Acharya B, Dutta A, Basu P. Chemical-looping gasification of biomass for hydrogen-enriched gas. *Energy and Fuels* 2009; 23(10): 5077–5083. doi: 10.1021/ef9003889

32. Silvester L, Antzara A, Boskovic G, Heracleous E, Lemonidou AA, Bukur DB. NiO supported on Al2O3 and ZrO2 oxygen carriers for chemical looping steam methane reforming. *International Journal of Hydrogen Energy* 2015; 40(24): 7490–7501. doi: 10.1016/j.ijhydene.2014.12.130

33. Ryden M, Lyngfelt A, Mattisson T. Synthesis gas generation by chemical-looping reforming in a continuously operating laboratory reactor. *Fuel* 2006; 85(12-13): 1631–1641. doi: 10.1016/j.fuel.2006.02.004

34. Dou J, Krzystowczyk E, Mishra A, Liu X, Li F. Perovskite Promoted Mixed Cobalt-Iron Oxides for Enhanced Chemical Looping Air Separation. *ACS Sustainable Chemistry and Engineering* 2018; 6(11): 15528–15540. doi: 10.1021/acssuschemeng.8b03970

35. Vieten J, Bulfin B, Call F, et al. Perovskite oxides for application in thermochemical air separation and oxygen storage. *Journal of Materials Chemistry A* 2016; 4(35): 13652–13659. doi: 10.1039/c6ta04867f

36. Song T, Shen L. Review of reactor for chemical looping combustion of solid fuels. *International Journal of Greenhouse Gas Control* 2018; 76(June): 92–110. doi: 10.1016/j.ijggc.2018.06.004

37. Noorman S, Van Sint Annaland M, Kuipers H. Packed bed reactor technology for chemical-looping combustion. *Industrial and Engineering Chemistry Research* 2007; 46(12): 4212–4220. doi: 10.1021/ie061178i

38. Burrows L, Gao PX, Bollas GM. Thermodynamic feasibility analysis of distributed chemical looping ammonia synthesis. *Chemical Engineering Journal* 2021; 426(May): 131421. doi: 10.1016/j.cej.2021.131421

39. Zhou Z, Han L, Bollas GM. Kinetics of NiO reduction by H2 and Ni oxidation at conditions relevant to chemical-looping combustion and reforming. *International Journal of Hydrogen Energy* 2014; 39(16): 8535–8556. doi: 10.1016/j.ijhydene.2014.03.161

40. Han L, Zhou Z, Bollas GM. Heterogeneous modeling of chemical-looping combustion. Part 1: Reactor model. *Chemical Engineering Science* 2013; 104: 233–249. doi: 10.1016/j.ces.2013.09.021

41. E & P Forum . Methods for Estimating Atmospheric Emissions from E&P Operations. The Oil Industry International Exploration & Production Forum Report No 2.59/197. tech. rep., 1994.

42. Doumbia EHT, Liousse C, Keita S, et al. Flaring emissions in Africa: Distribution, evolution and comparison with current inventories. *Atmospheric Environment* 2019; 199(November 2018): 423–434. doi: 10.1016/j.atmosenv.2018.11.006

43. Gilmer LK, Caico CA, Sherrick JJ, Mueller GR, Loos KR. Texas Commission on Environmental Quality Work Assignment 5 Draft Flare Waste Gas Flow Rate and Composition. tech. rep., Shell Global Solutions; Houston, TX: . https://www.emnrd.nm.gov/ocd/wp-content/uploads/sites/6/TCEQ-DraftWasteFlareFlowRatemeasurement.pdf. Accessed November 10 2021.

44. Zhou Z, Han L, Bollas GM. Model-based analysis of bench-scale fixed-bed units for chemical-looping combustion. *Chemical Engineering Journal* 2013; 233: 331–348. doi: 10.1016/j.cej.2013.08.025

45. Zhou Z, Han L, Nordness O, Bollas GM. Continuous regime of chemical-looping combustion (CLC) and chemical-looping with oxygen uncoupling (CLOU) reactivity of CuO oxygen carriers. *Applied Catalysis B: Environmental* 2015; 166-167: 132–144. doi: 10.1016/j.apcatb.2014.10.067

46. Nordness O, Han L, Zhou Z, Bollas GM. High-Pressure Chemical-Looping of Methane and Synthesis Gas with Ni and Cu Oxygen Carriers. *Energy and Fuels* 2016; 30(1): 504–514. doi: 10.1021/acs.energyfuels.5b01986

47. Han L, Zhou Z, Bollas GM. Model-Based Analysis of Chemical-Looping Combustion Experiments. Part I: Structural Identifiability of Kinetic Models for NiO Reduction. *AIChE Journal* 2016; 62(7): 2419–2431. doi: 10.1002/aic

48. Han L, Zhou Z, Bollas GM. Model-Based Analysis of Chemical-Looping Combustion Experiments. Part II: Optimal Design of CH4-NiO Reduction Experiments. *AIChE Journal* 2016; 62(7): 2432–2446. doi: 10.1002/aic

49. Han L, Zhou Z, Bollas GM. Heterogeneous modeling of chemical-looping combustion. Part 2: Particle model. *Chemical Engineering Science* 2014; 113: 116–128. doi: 10.1016/j.ces.2014.03.030

50. García-Labiano F, Adánez J, Diego dLF, Gayán P, Abad A. Effect of pressure on the behavior of copper-, iron-, and nickel-based oxygen carriers for chemical-looping combustion. *Energy and Fuels* 2006; 20(1): 26–33. doi: 10.1021/ef050238e

51. Scognamiglio D, Russo L, Maffettone PL, Salemme L, Simeone M, Crescitelli S. Modeling temperature profiles of a catalytic autothermal methane reformer with nickel catalyst. *Industrial and Engineering Chemistry Research* 2009; 48(4): 1804–1815. doi: 10.1021/ie800518e

52. McDaniel M, Tichenor BA. Flare Efficiency Study. tech. rep., US Environmental Protection Agency; Washington, DC: 1983. EPA/600/2-83/052 (NTIS PB83261644).

543 53. Mattisson T, Johansson M, Lyngfelt A. The use of NiO as an oxygen carrier in chemical-looping combustion. *Fuel* 2006;
544 85(5-6): 736–747. doi: 10.1016/j.fuel.2005.07.021

545 54. Process Systems Enterprise . gPROMS. online; 1997-2022. www.psenterprise.com/products/gproms.

546 55. Jarvis RB. *Robust Dynamic Simulation of Chemical Engineering*. PhD thesis. Imperial College, London; 1993.